5 Numerical Results

In this chapter, we give various examples illustrating the performance of the monotone multigrid method for frictionless contact problems. As it turns out, the monotone multigrid method shows to be a reliable and efficient solver for nonlinear contact problems. It combines the benefits of standard linear multigrid methods with the advantages of a highly accurate and a globally convergent nonlinear solver.

Before giving the numerical examples, let us discuss what particular aspects of the numerical experiments we are interested in.

The first one to be considered is the accuracy of the solution. Since contact stresses are of primary interest in many applications, see, e.g., [ARS99], we start with a Hertzian Contact Problem, where the analytical solution is known from [Her82], see also [KO88, p. 141]. The computed boundary stresses are in excellent agreement with those known from the analytical solution even for a small number of unknowns. This is due to the discrete solution satisfying the non-penetration condition exactly. For a comparison of the boundary stresses computed using a penalty method with the analytical ones, we refer the reader to [ESW99].

In view of Theorem 3.5, we distinguish between the *transient* and the *linear* phase of the iteration process. Within the transient phase, the discrete zone of contact is searched whereas within the linear phase the discrete zone of contact is known and the asymptotic linear problem is solved. The numerical examples presented in this chapter are intended to illustrate the *quantitative* aspects of our method within the transient as well as within the linear phase.

Theorem 3.3 provides the global convergence of our monotone multigrid method. This theoretical result is of particular importance for the transient phase. However, no upper bound for the convergence rate is available. Moreover, the convergence speed within the nonlinear phase depends strongly on the start iterate $\boldsymbol{u}_0^j$. To illustrate this effect, we take $u_k^0 = 0$ and $\boldsymbol{u}_0^k = \mathcal{I}_{k-1}^k \tilde{\boldsymbol{u}}^{k-1}$ as resulting from nested iteration in our numerical examples. Here, $\mathcal{I}_{k-1}^k \colon \boldsymbol{S}^{(k-1)} \longrightarrow \boldsymbol{S}^{(k)}$ denotes the canonical injection.

Once the discrete zone of contact has been identified, the nonlinear problem reduces to a linear problem with mixed boundary conditions. Thus, it would be possible to apply a standard linear multigrid method. However, this requires an additional setup phase for the multigrid method. In particular, the stiffness matrices have to be reassembled. Thus, we do not proceed in this way and rather use the extended splitting (3.1). This is justified, if the convergence speed of the multigrid method induced by (3.1) is comparable with that of a standard multigrid solver applied to the asymptotic linear problem. Our numerical examples show, that the convergence speed of our truncated monotone multigrid method is comparable to standard multigrid methods applied to the corresponding linear problem with known boundary data. That is, applying the nonlinear monotone multigrid method to a linear problem yields the convergence behavior of a fast linear solver.

Moreover, we consider the effect of varying normals. Since we assume small displacements, the non-penetration condition can be given with respect to the outer normals of the body $\mathscr{B}$ as well as with respect to the outer normals of the rigid foundation, see Section 2.1. In particular, we consider the contact of a body with constant outer normal at Γ_S with an obstacle with curvilinear boundary. This allows us to compare the case

of equal normals with the case of varying normals for almost the same problem, i.e., the same *linearized* problem. Finally in Section 5.2, we consider an example with large deformations. Here, nearly "opposite" displacements are represented by a *single* coarse grid function. As it turns out, this does not affect the speed of convergence.

To summarize, we are interested in the following points:

- quality of the solution, i.e., accuracy of the computed boundary stresses,
- convergence speed within the nonlinear or transient phase of the iteration process, in particular, influence of the start iterate,
- convergence speed within the linear phase of the iteration process, in particular, comparison with standard multigrid methods,
- influence of varying normals at the Signorini boundary.

For the case of frictional contact problems, we refer the reader to Section 6.3. Let us start with a simple example in two space dimensions, where the analytical solution is known.

5.1 Hertzian Contact Problem

In our first example, we consider a plane strain problem for a half circle centered at $(0, 0.4)$ with radius 0.4 in elastic contact with a rigid plane. The material of the half circle is assumed to be homogeneous and isotropic with Young's modulus $E = 270269$ N/mm^2 and Poisson's ratio $\nu = 0.248$. We prescribe vertical displacement $u(x, y) = -0.005$ at $\Gamma_D = \{(x, y) \in \Gamma \mid y = 0.4\}$ and the Signorini boundary conditions (2.12) at $\Gamma_S = \partial\mathscr{B} \setminus \Gamma_D$. The continuous problem is discretized by linear and bilinear finite elements on triangles and quadrilaterals, respectively. In this example, normals $\boldsymbol{n}_J(p) = \boldsymbol{n}(p)$, $p \in \mathcal{N}^{(J)}$, are chosen to be the outer normal of the plane. An example with varying normals will be given in the next section.

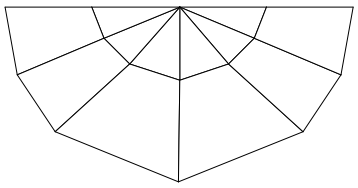

Figure 5.1: Initial partition $\mathcal{T}_0$

Starting with the initial partition $\mathcal{T}_0$ as depicted in Figure 5.1, a sequence of triangulations $\mathcal{T}_0, \ldots, \mathcal{T}_J$, $J = 11$, is produced by adaptive refinement. The adaptive refinement process is controlled by a locally defined error indicator. Following the lines of [Kor96], we use a hierarchical approach. Since $\mathscr{B}$ is not resolved by the coarse grid, new nodes are moved onto the boundary $\partial\mathscr{B}$.

For the iterative solution of the discrete problems, we use the fully truncated variant of our monotone multigrid method as described at the end of the preceeding chapter, i.e., Algorithm 1. On each level $k > 0$, we apply 4 pre- and 4 post-smoothing steps. Problems on Level 0 are solved up to machine precision by a projected block Gauß–Seidel iteration. On subsequent levels, $k \geq 1$, the iterate $\tilde{\boldsymbol{u}}_k = \boldsymbol{u}_k^{\nu+1}$ is accepted, if the stopping criterion

$$\|\boldsymbol{u}_k^{\nu+1} - \boldsymbol{u}_k^{\nu}\|_a \leq 0.05\, \sigma_{\text{alg}} \sigma_{\text{app}} \|\boldsymbol{u}_k^{\nu}\|_a \tag{5.1}$$

is satisfied with safety parameters $\sigma_{\text{alg}} = 1$, $\sigma_{\text{app}} = 0.1$. Here, $\|\cdot\|_a^2 = a(\cdot,\cdot)$ denotes the energy norm. As a consequence, the estimated algebraic error does not interfere with the estimated discretization error on the final level (cf. [Kor97b], pp. 108). We choose initial iterates $u_k^0 = \mathcal{I}_{k-1}^k \tilde{u}_{k-1}$ for $k = 1, \ldots, 11$ (nested iteration). The resulting approximation history is reported in Table 5.1. It turns out that only 3 iteration steps are required on

level	# dof	# iterations	# coincidence set	estimated relative errors	
				displacements	normal stress
0	30	–	1	64.93	72.12
1	78	3	1	46.68	58.48
2	146	3	1	37.52	33.31
3	222	3	3	18.20	7.54
4	508	3	5	12.52	0.47
5	1 016	3	7	7.51	0.52
6	2 220	3	15	4.77	0.33
7	5 600	3	29	2.91	0.21
8	13 032	3	51	1.92	0.22
9	39 976	3	89	1.10	0.20
10	67 274	3	119	0.84	0.20
11	109 534	3	161	0.65	0.20

Table 5.1: Approximation history

each refinement level. The error of the displacements is measured in the energy norm. Note that the estimated error is proportional to $n_k^{1/2}$ which is in good agreement with the $\mathcal{O}(h)$ estimate (2.29) and Jackson's inequality (2.26) for $s = 1$. In Figure 5.2, the estimated relative error (blue crosses) and the expected asymptotic behavior from (2.26) for $s = 1$ of the error (red circles) is depicted. The underlying hierarchy of tringulations is illustrated in Figure 5.3. The color reflects the meshsize, ranging from red (small elements) to blue (large elements). Observe that the red spots of strong local refinement in the final triangulation $\mathcal{T}_{11}$ coincide with the boundary of the contact set.

Final approximation of tangential (red) and normal boundary stress (blue) is depicted in Figure 5.4. We emphasize that the tangential stresses are zero up to an algebraic error which could be reduced down to machine precision by sufficiently many multigrid iterations. We now check the accuracy of the normal stress. Following [Her82], see also [KO88, p. 141], normal contact stresses can be computed analytically from the Hertz solution. Approximating the width of the contact surface of u by the width of the contact

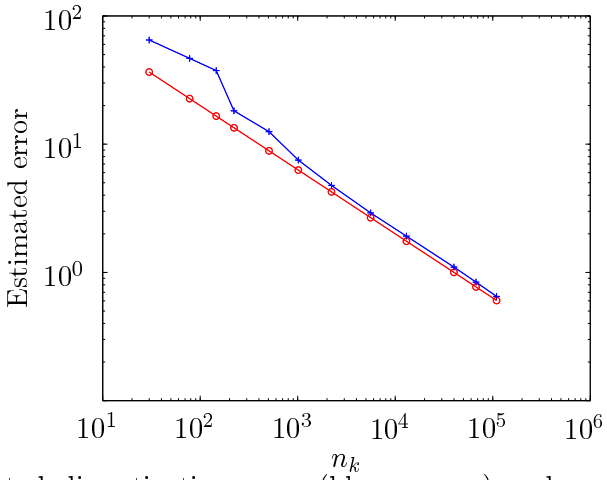

Figure 5.2: Estimated discretization error (blue crosses) and $c \cdot n_k^{-1/2}$ (red cirlces) vs. number of unknowns (n_k)

surface of the discrete solution $\boldsymbol{u}_{11}$ an approximate Hertzian normal contact stress can be computed analytically. As it is standard, see, e.g. [CSW99, Wri95], this approximation of the Hertzian contact stress is taken as reference solution. The last column of Table 5.1 contains the relative deviation of the maximal normal stress of $\tilde{u}_k$ from the maximal Hertzian normal stress. Both coincide up to an error of less than 0.5% for $k = 4$. Let us emphasize that the coincidence set contains only 5 nodes on this level. In particular, a good approximation of the maximal normal stress can already be obtained after a small number of refinement steps. We note that the analytical solution of Hertz is based on a parable and not a half circle [Wri00]. Thus, we cannot expect that the relative error in the normal stress tends to zero for high level number. The impressive overall accuracy is a consequence of our discrete approach which *does not involve any relaxation of contact conditions*. This is in contrast to, e.g., penalty methods.

We now investigate the convergence behavior of our multigrid method on the final grid $\mathcal{T}_{11}$. The left picture of Figure 5.5 shows the algebraic error $\|\boldsymbol{u}_{11} - \boldsymbol{u}_{11}^{\nu}\|_a$ for $\nu = 0, \ldots, 33$. The red curve is obtained using the initial iterate $\boldsymbol{u}_{11}^0 = \mathcal{I}_{10}^{11}\tilde{u}_{10}^3$ (nested iteration). We observe linear convergence throughout the iteration. In fact, the exact discrete coincidence set is detected after one iteration step. Leading high convergence speed is due to fast reduction of the high frequency contributions of the error. The blue curve illustrates the iteration history for the (artificial) initial iterate $\boldsymbol{u}_{11}^0 = 0$. In this case the discrete coincidence set is detected after 10 iterations. In spite of leading fully nonlinear iterations we observe again a linear reduction of the error throughout the iteration. This effect is not typical, see, e.g., next section or [Kor97a], but reflects the simplicity of the Hertzian model problem under consideration.

In our final experiment, we compute approximate *asymptotic convergence rates* ρ_k

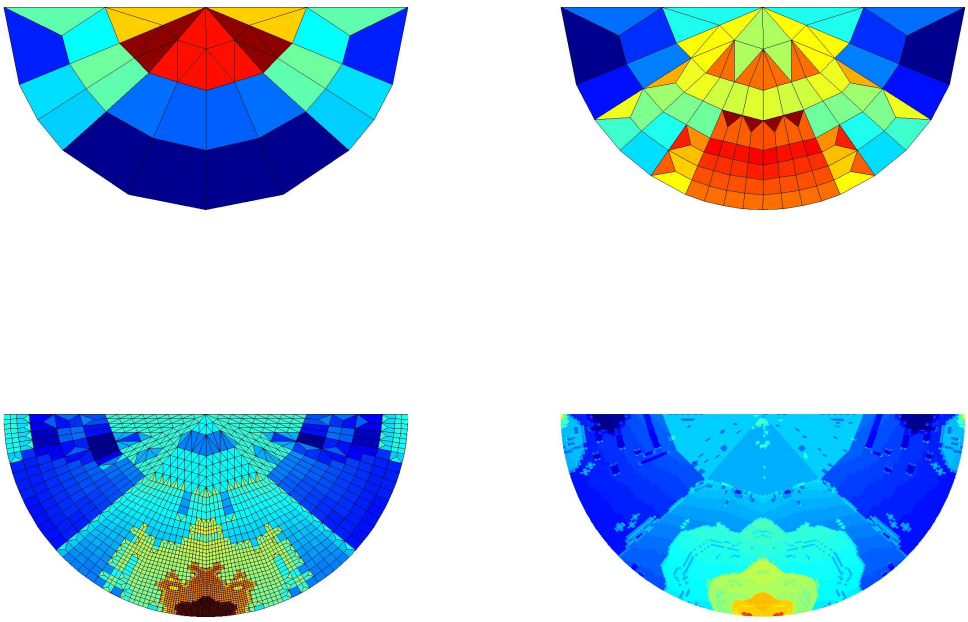

Figure 5.3: Refinement history for partitions $\mathcal{T}_j$ for $j = 1, 3, 7, 11$.

according to

$$\rho_k = \frac{\|\boldsymbol{u}_k^{\nu^*+1} - \boldsymbol{u}_k^{\nu^*}\|_a}{\|\boldsymbol{u}_k^{\nu^*} - \boldsymbol{u}_k^{\nu^*-1}\|_a} \tag{5.2}$$

on each level, $k = 0, \ldots, 11$. Here, ν^* is chosen such that

$$\|\boldsymbol{u}_k^{\nu^*+1} - \boldsymbol{u}_k^{\nu^*}\|_a < 10^{-12} \ .$$

The asymptotic convergence rates are computed for the $\mathcal{V}(4,4)$- and the $\mathcal{W}(4,4)$-cycle. As illustrated by the middle picture in Figure 5.5, asymptotic convergence rates seem to saturate at about $\rho_\infty = 0.4$ for the $\mathcal{V}$-cycle (middle) and at about $\rho_\infty = 0.1$ for the $\mathcal{W}$ cycle (right) for increasing levels $k \to \infty$.

5.2 An Unphysical Example

In this section, our goal is to study the behavior of our algorithm in case of highly varying normals. Since the extended splitting (3.1) depends on the outer normals, we study the influence of the outer normals on the convergence speed of the method. Let us note

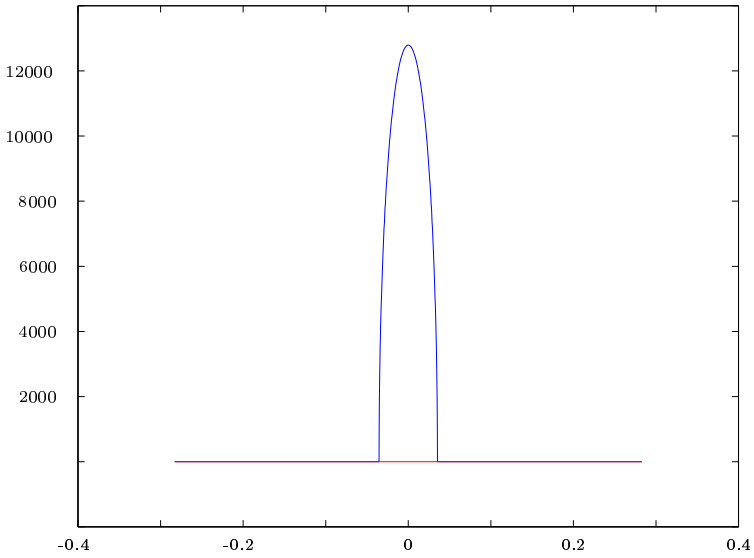

Figure 5.4: Final approximation of boundary stress at Γ_S

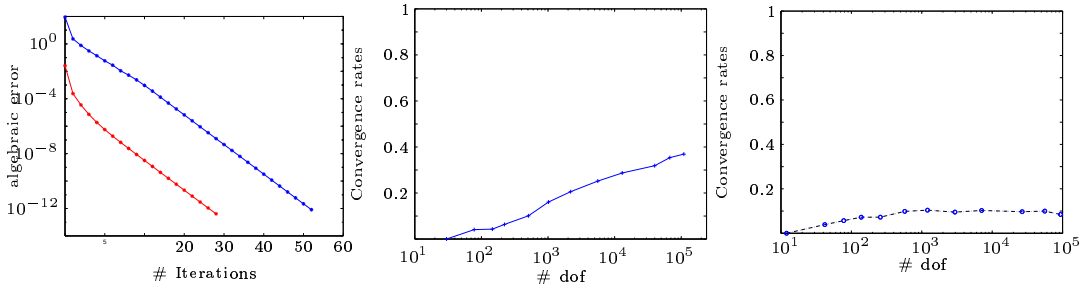

Figure 5.5: Iteration history on Level $J = 11$ and asymptotic convergence rates for the $\mathcal{V}(4,4)$-cycle (left) and $\mathcal{W}(4,4)$-cycle (right)

that by construction, the truncated basis functions on the coarsest grid can be used to represent displacements in arbitrary directions. Concerning the example given in this section, the *single* coarse grid function associated with the Signorini boundary represents nearly "opposite" displacements. As a matter of fact, this does not affect the convergence speed of the monotone multigrid method. The monotone multigrid method shows to be robust with respect to highly varying normals.

Here, we consider a contact problem with large deformations but assume linear elasticity. Obviously, this is not covered by the assumptions made in Chapter 1, in particular, (1.2) is violated. Although this problem has to be considered as "unphysical", it illustrates the behavior of our method in case of highly varying normals. The body $\mathscr{B}$ to be deformed is the unit square. At the right and left boundary, we prescribe homogeneous Neumann boundary conditions. The lower boundary is the Signorini boundary Γ_S. We prescribe displacements of $u(x, y) = (-0.6, 0)$ at the upper boundary of the quadrilateral.

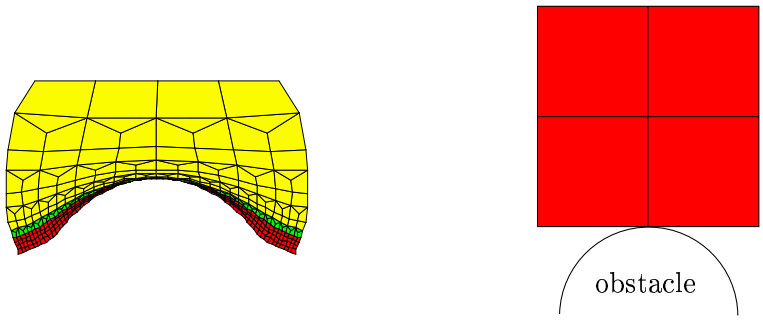

Figure 5.6: Deformation with higly varying normals (left) and initial triangulation (right)

The obstacle is a rigid circular arc with radius 0.4, see the right picture in Figure 5.6. Here, the initial triangulation and the osbtacle are depicted. The material parameters are $E = 206000$ and $\nu = 0.28$. The resulting deformation and the initial triangulation are shown in Figure 5.6. For completeness, the computed boundary stresses are depicted in Figure 5.7. At the endpoints of the actual contact zone we have outer normals which are

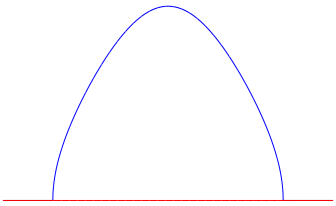

Figure 5.7: Boundary stresses

almost linearly dependent but have opposite sign. In particular, the coarse grid correction originating from minimization in direction of $\boldsymbol{\mu}^0_{(0,0.5)} \in \boldsymbol{S}^{(0)}$ contributes to displacements in direction of nearly "opposite" normals $\boldsymbol{n}_p, \boldsymbol{n}_q$, $p, q \in \mathcal{N}^{(J)^\bullet}(\bar{\boldsymbol{u}}^\nu_J)$, i.e., $\boldsymbol{n}_p \cdot \boldsymbol{n}_q \approx -1$. The resutling asymptotic convergence rates are depicted in Figure 5.8. As it can be seen, the method behaves as in the case of constant normal directions.

5.3 Elastic Cylinder and Two Rigid Rods

In this section, we consider a highly nontrivial example in three space dimensions, illustrating the flexibility and efficiency of our method. The numerical simulation of a nonlinear contact problems in three space dimensions is a highly challenging task. We consider the

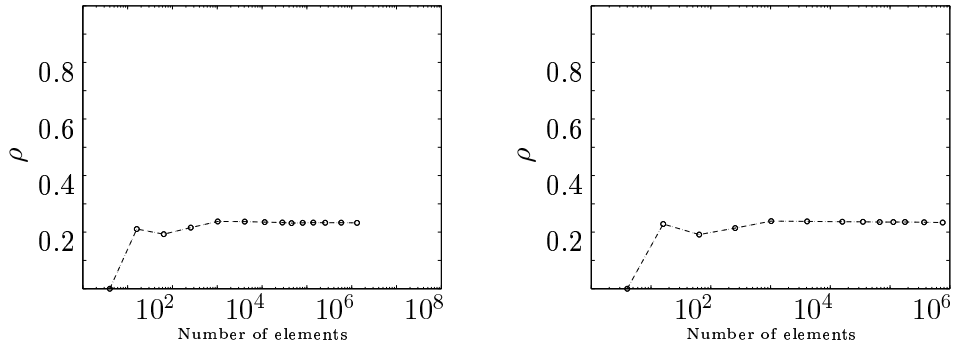

Figure 5.8: Asymptotic convergence rates for the $\mathcal{W}(1,1)$-cycle with highly varying normals (left) and with constant normals (right)

deformation of an elastic cylinder with axis $\{(x,y,z)\,|\,y=0.5,\ z=1.0\}$, radius 1 and length one against two rigid cylindrical rods with axis $\{(x,y,z)\,|\,x=0.25,\ z=-0.25\}$ and $\{(x,y,z)\,|\,x=0.75,\ z=-0.25\}$, respectively, radius 0.25 and infinite length. We choose homogeneous and isotropic material with Young's modulus $E = 206000\ \mathrm{N/mm^2}$ and Poisson's ratio $\nu = 0.28$. Dirichlet boundary conditions $u(x,y) = -0.05$ are prescribed at $\Gamma_D = \{(x,y,z) \in \partial\mathscr{B} \mid z \geq 0.75\}$ and Signorini boundary conditions at $\Gamma_S = \{(x,y,z) \in \partial\mathscr{B} \mid z \leq 0.25\}$. The remaining part of the boundary satisfies homogeneous Neumann boundary conditions. In Figure 5.9, a cross section is depicted, illustrating the position of the two rods. The continuous problem is discretized by trilin-

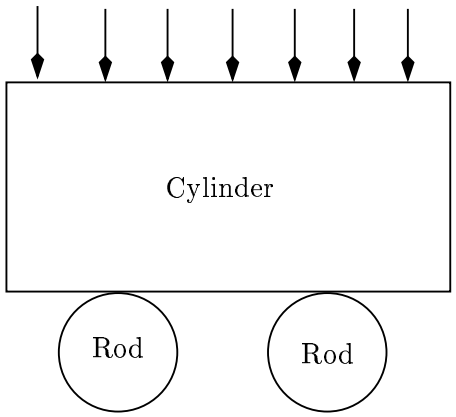

Figure 5.9: Cylinder and obstacles — cross section

ear finite elements on quadrilaterals. The normals $\boldsymbol{n}_J(p) = \boldsymbol{n}(p)$, $p \in \mathcal{N}^{(J)}$, are directed in radial direction of the cylinder. The initial partition $\mathcal{T}_0$ is shown in Figure 5.10. Again, we produce a sequence $\mathcal{T}_0, \ldots, \mathcal{T}_J$, $J = 5$, by successive local refinement moving new nodes at the boundary onto $\partial\mathscr{B}$. In order to maximize the significance of the nonlinearity at Γ_S in the discrete problem, only those elements having at least one vertex $p = (p_x, p_y, p_z)$ with $p_z < 0.04$ are refined in each step. Again, we consider the fully truncated monotone

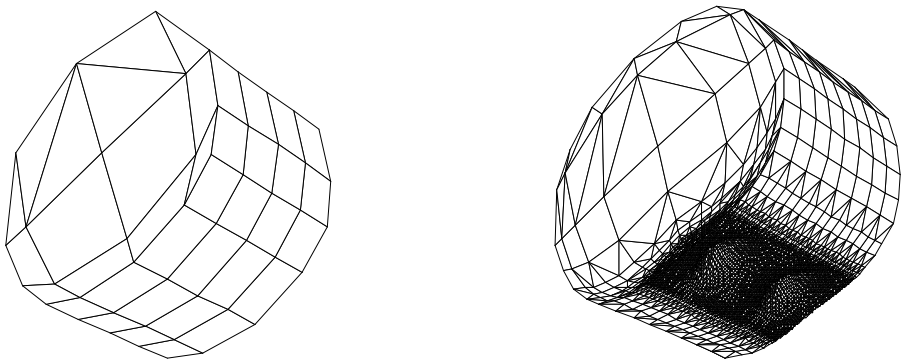

Figure 5.10: Initial partition $\mathcal{T}_0$ and deformed final partition $\mathcal{T}_5$

multigrid with 4 pre– and 4 post–smoothing steps, and the coarse grid problems on Level 0 are solved up to machine precision.

The deformed final partition $\mathcal{T}_5$ is shown in the right picture of Figure 5.10, the final approximation of contact stress is shown in Figure 5.11. We recall that the condition $\sigma_T = 0$ is fulfilled up to algebraic accuracy, and that in contrast to penalty methods, the error of the computed boundary stresses depends only on the algebraic accuracy and the discretization error (2.29), but not on any additional parameters. The convergence history on the final grid $\mathcal{T}_5$ is shown in the left picture of Figure 5.12. Again the red curve corresponds to nested iteration. As in the twodimensional example given in Section 5.1, the resulting initial iterate is sufficiently accurate to enter the asymptotic regime immediately. This is different for the artificial guess $\boldsymbol{u}_5^0 = 0$. As illustrated by the blue curve, it takes about 50 transient steps to reach the asymptotic regime. Note that the asymptotic convergence rates are the same, as predicted by Theorem 3.5. We remark, that it is possible to shorten the initial transient phase by various heuristic strategies, e.g., by additional truncation in case of very small absolute values of the quasioptimal obstacles $(\overline{\psi}_p^{(k)})^i$, $(\underline{\psi}_p^{(k)})^i$. Using a $\mathcal{W}$-cycle instead of $\mathcal{V}$-cycle also shortens the transient phase. In order to illustrate the convergence behavior for decreasing meshsize, we compute approximate asymptotic convergence rates ρ_k, $k = 0, \ldots, 5$, according to (5.2). The right picture in Figure 5.12 indicates that asymptotic convergence rates saturate at about $\rho_\infty = 0.65$ for increasing levels $k \to \infty$. Similar results are observed for classical multigrid methods as applied to unconstraind problems. Indeed, prescribing boundary stresses as depicted in Figure 5.11 instead of constraints and applying a standard multigrid solver from UG, we obtain almost the same aymptotic convergence rates.

In the following section, we consider in detail the relation of our monotone multigrid method to a standard linear multigrid. A comparison in the asymptotic linear phase is given and discussed. Numerical results illustrate the flexibility and efficiency of our

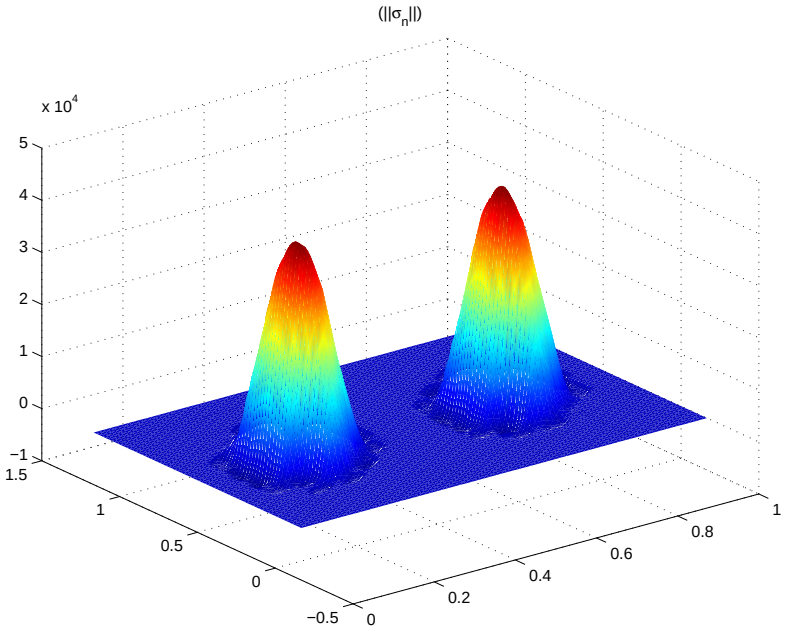

Figure 5.11: Final approximation of boundary stress at Γ_S

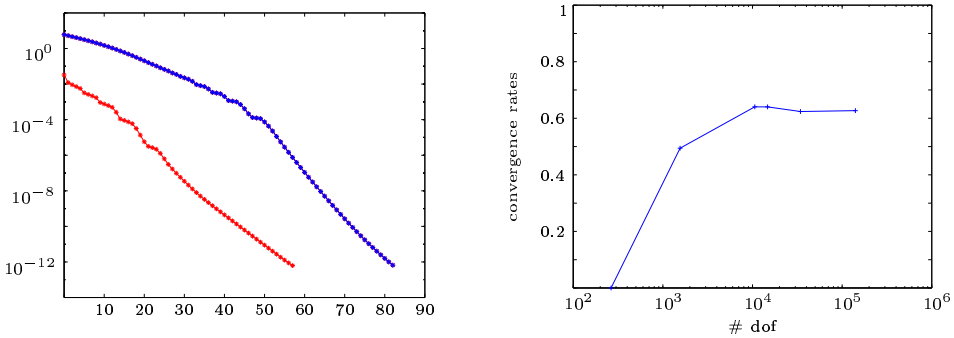

Figure 5.12: Iteration history on level $J = 5$ and asymptotic convergence rates

method.

5.4 Comparison with Standard Multigrid

Since the pioneering work [Osw90] of Oswald, who was the first to realize the strong link between approximation theory and multigrid convergence theory, multigrid methods are known to be optimal for elliptic partial differential equations. Unfortunately, these results cannot be used directly for a *quantitave* analysis of multigrid methods, since the constants depend on the geometry of the domain and are in general not available.

In this section, we compare our monotone multigrid with a standard multigrid method applied to the *linear* problem, which is related to each Signorini problem. Our aim is to compare the convergence speed of the monotone multigrid method within the linear phase to the convergence speed of a standard linear solver. We proceed as follows: After solving the Signorini problem, on each level we take the computed boundary stresses as Neumann boundary data for the linear multigrid method. This is done on each refinement level and allows us to compare the quantitative behaviour of the standard multigrid with that of the monotone method. As it turns out, our truncated monotone multigrid method shows to be as efficient as a standard linear multigrid solver. In particular, using nested iteration, we can solve a nonlinear contact problem nearly as fast as a linear problem *with given boundary data*.

We start with a Hertzian contact problem in three space dimensions. Here, a ball with radius one and midpoint $(0.5, 0.5, 0.5)$ is pressed against the plane $\{z = -0.5\}$. The initial distance of the ball to the plane is zero, i.e., in the reference configuration there is contact at exactly one point of Γ_S. The material parameters are $E = 2000$ und $\nu = 0.25$. Dirichlet boundary conditions $u(x, y) = -0.05$ are prescribed at $\Gamma_D = \{(x, y, z) \in \partial\mathscr{B} \mid z \geq 1.25\}$ and Signorini boundary conditions at $\Gamma_S = \{(x, y, z) \in \partial\mathscr{B} \mid z \leq -0.25\}$. The remaining part of the boundary satisfies homogeneous Neumann boundary conditions. The normals are choosen to be the outer normals of the ball, i.e., we have varying normals at the contact boundary. The deformed configuration scaled by a factor of 5 can be seen in the right of Figure 5.4. Again, due to the scaling, the shape of the obstacle is not reproduced. To compare our monotone multigrid method with the standard multigrid method, we proceed as follows on each level. We compute the solution to Signorini's problem using our truncated monotone multigrid method. Then, the computed stresses at the contact boundary are used as Neumann boundary data for the linear solver. The asymptotic linear convergence rates are compared, using a $\mathcal{W}(3, 3)$-cycle for both methods. The initial iterate is the same for both methods and is taken to be $\boldsymbol{u}_k^0 = \mathcal{I}_{k-1}^k \tilde{u}_{k-1}$. We remark, that the linear multigrid is not able to handle Neumann boundary conditions given with respect to the normal/tangential coordinate system. Thus, the computed boundary stresses are transformed to the standard basis $\{\boldsymbol{E}_i\}$ of $\mathbb{R}^3$. We use adaptive refinement controlled by a residual based error indicator, thus stressing the nonlinearity at the contact boundary. A cross section of the resulting Grid ob Level 5 can be seen in Figure 5.4. Note the highly local refinement in the contact region. In Table 5.2, the asymptotic convergence rates of the nonlinear and the linear method, the number of unknowns and the number of contact nodes are given. For convenience, in Figure 5.14 the asymptotic convergence rates ρ_{MMG} and ρ_{STDMG} of the nonlinear and the linear

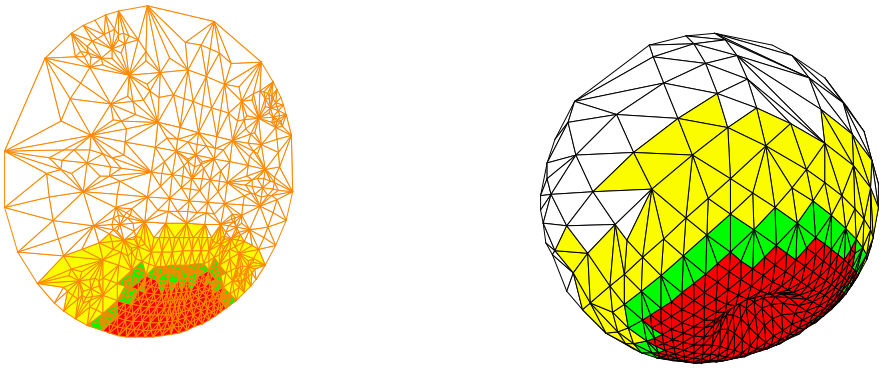

Figure 5.13: Cross section of the mesh on Level 5 (left) and deformed body (right)

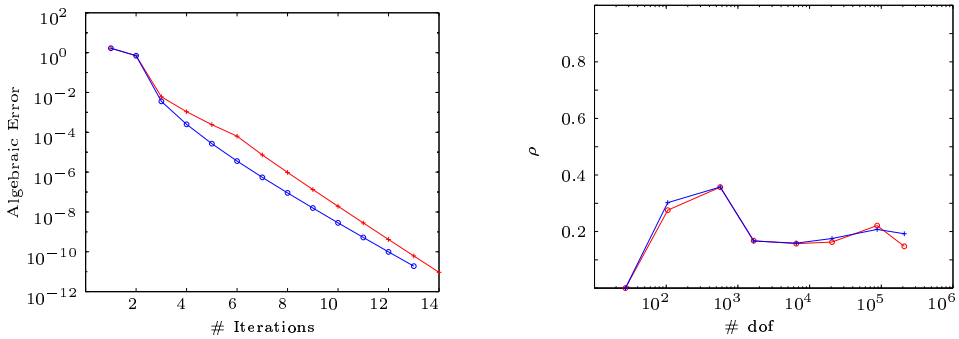

Figure 5.14: Comparison of the monotone multigrid method (red) and the standard linear multigrid method with given boundary data (blue): Asymptotic convergence rates (left) and iteration history on Level 7 (right)

method are depicted. As can be seen, there is nearly perfect agreement of the convergence rates. Thus, our monotone multigrid method shows to be a fast and efficient solver even for the asymptotic linear problem. Let us emphasize, that we have solved a nonlinear contact problem with varying normals with computational amount comparable to that of a standard method for the case of *known boundary data*. In the left of Figure 5.14, also the iteration history on Level 7 is shown, i.e., the estimated algebraic error versus the number of unknowns. The initial slowdown of the monotone multigrid method (red crosses) is due to the nonlinearity. As soon as the contact boundary has been identified, the asymptotic linear regime starts. In particular, there is only *one* additional iteration necessary to resolve the nonlinearity. Our next example is the Hertzian contact problem presented in Section 5.1. Here, we do not only consider the $\mathcal{V}$-cycle as in Section 5.1, but also the $\mathcal{W}$-cycle. Adaptive refinement is contolled by the hierarchical error estimator. In contrast to Section 5.1, here on each level the algebraic error, measured in the energy norm, is reduced up to an estimated error of 10^{-12}. Thus, the grid hierarchy is slightly different from that used in Section 5.1, see Table 5.3. As can be seen in Figure 5.4, the

Level	# dof	# coincidence set	ρ_{MMG}	ρ_{STDMG}
0	9	0	—	—
1	35	1	$2.7 \cdot 10^{-1}$	$3.0 \cdot 10^{-1}$
2	189	1	$3.5 \cdot 10^{-1}$	$3.5 \cdot 10^{-1}$
3	554	5	$1.6 \cdot 10^{-1}$	$1.6 \cdot 10^{-1}$
4	2 173	9	$1.6 \cdot 10^{-1}$	$1.6 \cdot 10^{-1}$
5	6 843	45	$1.6 \cdot 10^{-1}$	$1.7 \cdot 10^{-1}$
6	29 203	177	$2.2 \cdot 10^{-1}$	$2.0 \cdot 10^{-1}$
7	69 877	620	$1.5 \cdot 10^{-1}$	$1.9 \cdot 10^{-1}$

Table 5.2: Comparison of monotone multigrid method ρ_{MMG} and standard linear multigrid method ρ_{STDMG} for the threedimenional example

asymptotic convergence rates of the monotone multigrid method of the $\mathcal{V}(3,3)$-cycle and of the $\mathcal{W}(3,3)$-cycle are comparable to the corresponding asymptotic convergence rates of the standard multigrid method. For both methods, the results obtained by using the $\mathcal{W}(3,3)$-cycle are better than those obtained by using the $\mathcal{V}(3,3)$-cycle, see Figure 5.4 or Table 5.3. Summarizing the results from both numerical experiments, we have shown

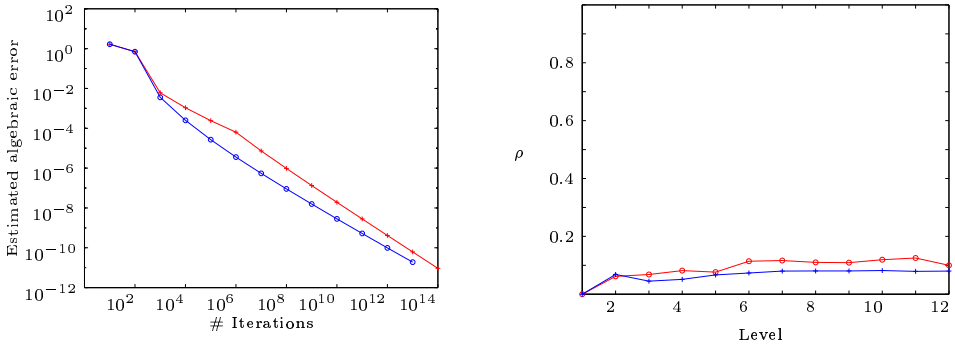

Figure 5.15: Comparison of the monotone multigrid method (red) and the standard linear multigrid method with given boundary data (blue) for the twodimensional example from Section 5.1: Asymptotic convergence rates (left) and iteration history on Level 7 (right)

that the *quantitative* behavior of our monotone multigrid methods is comparable to that of a standard multigrid method applied to a *linear problem with given boundary data*. Thus, our monotone multigrid method shows to be as efficient for *nonlinear* problems as standard multigrid methods are for *linear* problems.

5.5 Influence of the Start Iterate

In this section, we study the behavior of our monotone multigrid method in case of a bad start iterate. To this end, we consider a simplified model for a journal bearing. The geometry of the body in the reference configuration and the obstacle are depicted in Figure

Level	# dof	# coincidence set	ρ_{MMG}	ρ_{STDMG}
0	30	1	—	—
1	78	1	$6.17 \cdot 10^{-2}$	$6.84 \cdot 10^{-2}$
2	146	1	$6.84 \cdot 10^{-2}$	$4.53 \cdot 10^{-2}$
3	222	3	$8.15 \cdot 10^{-2}$	$5.14 \cdot 10^{-2}$
4	508	5	$7.63 \cdot 10^{-2}$	$6.68 \cdot 10^{-2}$
5	1 016	7	$1.14 \cdot 10^{-1}$	$7.32 \cdot 10^{-2}$
6	2 260	15	$1.16 \cdot 10^{-1}$	$7.99 \cdot 10^{-2}$
7	5 570	29	$1.10 \cdot 10^{-1}$	$8.05 \cdot 10^{-2}$
8	12 778	51	$1.09 \cdot 10^{-1}$	$8.04 \cdot 10^{-2}$
9	46 274	99	$1.19 \cdot 10^{-1}$	$8.17 \cdot 10^{-2}$
10	76 940	139	$1.25 \cdot 10^{-1}$	$7.90 \cdot 10^{-2}$
11	133 088	171	$1.07 \cdot 10^{-1}$	$7.69 \cdot 10^{-2}$

Table 5.3: Comparison of monotone multigrid method ρ_{MMG} and standard linear multigrid method ρ_{STDMG} for the twodimenional example

5.16. According to Figure 5.16, the bearing (red) is pressed against a circular obstacle. At the outer curvilinear boundary Γ_D of the bearing we prescribe Dirichlet values according to $u(x, y) = -\boldsymbol{n}(x, y) * 0.05$, where $\boldsymbol{n}(x, y)$ is the outer normal at the point $(x, y) \in \Gamma_D$. At the straight parts of the boundary, homogeneous Neumann boundary conditions are prescribed. The interior curvilinear boundary of the bearing is the Signorini boundary Γ_S. Here, the obstacle is given with respect to the outer normals at Γ_S. The radius of the bearing is $R_B = 0.5$ and the radius of the obstacle is $R_O = R_B - 10^{-8}$. The material parameters are $E = 206000$ and $\nu = 0.28$, which correspond to steel. As we have

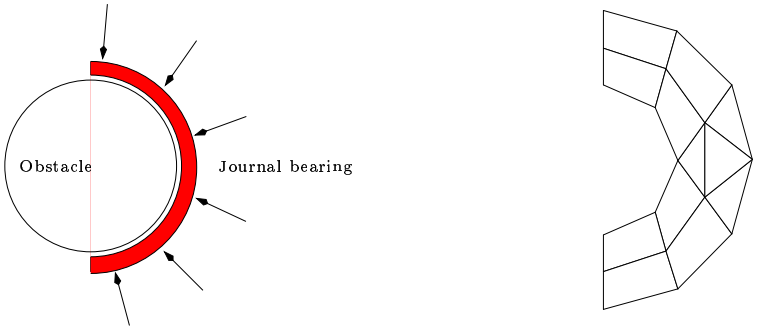

Figure 5.16: Geometry of the bearing model (left) and initial triangulation (right)

seen in the previous sections, in case of nested iteration the coincidence set is in general found within the first two iteration steps. Thus, for this example on each level j we use a randomly chosen initial iterate $\boldsymbol{u}_j^0$ with values $\boldsymbol{u}_i \in [-1, 1]$, $i = 1, 2$. For comparision, we also consider the initial iterate $\boldsymbol{u}_j^0 = 0$. Due to the physical interpretation of the model, we expect the actual zone of contact to coincide with the Signorini boundary.

This complicates the search for the coincidence set, since every coarse grid correction has to be admissible with respect to constraints given in the directions of highly varying normals. In particular, during the nonlinear phase the non penetration conditions in *normal* direction lead to constraints in *tangential* direction on the coarser grids. We use adaptive refinement controlled by the hierarchical error estimator. Since refinement takes primarily place near the Signorini boundary, see Figure 5.18, we have a large number of contact nodes compared with the number of inner nodes. Thus, with respect to the nonlinearity the problem can be considered as extremely difficult.

The numerical results are analyzed with respect to following criteria:

- number of nonlinear iterations until the coincidence set is found,
- number of total iterations until the prescribed tolerance is reached,
- speed of convergence in the nonlinear phase,
- asymptotic linear convergence speed.

We consider two different cases for the start iterate. In the first case, we chose $\boldsymbol{u}_j^0 = 0$ in the interior of the domain $\mathscr{B}$ and set $\boldsymbol{u}_j^0$ to random values taken from the interval $[-1,1] \times [-1,1]$ on Γ_S. In the second case, we set $\boldsymbol{u}_j^0 = \mathbf{0}$. On each level j, the iteration process is stopped, if the algebraic error $\|\boldsymbol{u}_j - \boldsymbol{u}_j^\nu\|_a$ measured in the energy norm is reduced up to a prescribed tolerance of 10^{-10}. Here, $\boldsymbol{u}_j$ stands for the exact solution on level j. We note, that we use the exact algebraic error. To compute the algebraic error, on each level the monotone multigrid method is applied twice. The first run provides the discrete solution $\boldsymbol{u}_j$, the second run provides the algebraic error. In Table 5.4, the number of nonlinear iterations to identify the coincidence set is shown. In round braces, the total number of iterations, i.e., *nonlinear and linear* is shown. As can be seen in Table 5.4,

Level	# dof	# contact	# nonlinear (total) iter. $\boldsymbol{u}_j^0\|_{\Gamma_S}$ rand.		$\boldsymbol{u}_j^0 = 0$		ρ
0	72	5	—	(—)	—	(—)	—
1	196	9	1	(8)	1	(6)	$3.54 \cdot 10^{-2}$
2	556	17	2	(10)	1	(8)	$6.70 \cdot 10^{-2}$
3	1808	33	2	(12)	1	(10)	$1.14 \cdot 10^{-1}$
4	4004	65	2	(13)	1	(9)	$1.34 \cdot 10^{-1}$
5	8 368	129	3	(12)	1	(9)	$6.85 \cdot 10^{-2}$
6	14 276	257	5	(13)	1	(9)	$6.82 \cdot 10^{-2}$
7	23 236	513	5	(13)	1	(9)	$6.94 \cdot 10^{-2}$
8	24 756	1 025	8	(16)	2	(9)	$5.98 \cdot 10^{-2}$
9	41 310	2 049	10	(18)	1	(9)	$5.64 \cdot 10^{-2}$
10	74 016	4 097	13	(20)	1	(9)	$6.09 \cdot 10^{-2}$

Table 5.4: Nonlinear behavior for different start iterates $\boldsymbol{u}_j^0$

the number of nonlinear iterations increases with increasing refinement level. However,

the total number of iterations required to reduce the algebraic error up to 10^{-10} does not increase proportionally. Comparing with the behavior of the method in case of the initial iterate $\boldsymbol{u}_j^0 = 0$, we see that a badly chosen initial iterate does slowdown the total iteration process. This is the case for any iterative method. Let us dicuss this point in more detail. From the iteration history on Level 8 depicted in Figure 5.18, we see that there is some "nonlinear convergence rate". For this example, it is about 0.7, i.e.,

$$\frac{\|\boldsymbol{u}_8^{\nu+1} - \boldsymbol{u}_j\|_a}{\|\boldsymbol{u}_8^{\nu} - \boldsymbol{u}_j\|_a} \approx 0.7$$

for $\nu \leq 8$. This is much slower than the asymptotic linear convergence rate of 0.1, but we observe constant reduction of the error during the nonlinear phase. A badly chosen initial iterate can slowdown the nonlinear iteration process, but it does not spoil the convergence speed in the nonlinear phase. Unfortunately, for the case of a randomly chosen initial iterate the number of nonlinear iterations increaes with increasing refinement level. This is also illustrated in Figure 5.17 The situation is different for the case $\boldsymbol{u}_j^0 = \boldsymbol{0}$. It is a

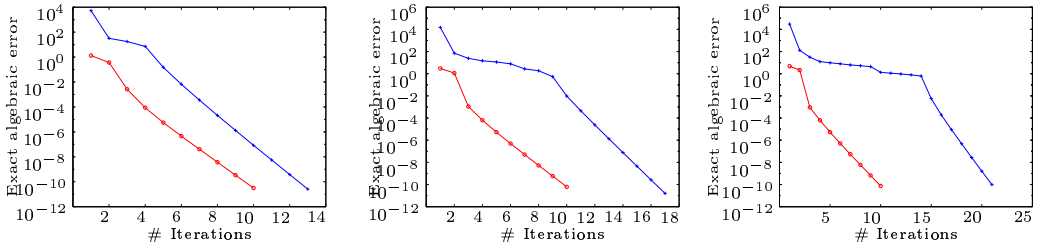

Figure 5.17: Iteration history on Level $j = 5, 8, 10$ for random initial iterate (blue) and zero initial iterate (red)

physically reasonable choice, since it corresponds to the undeformed configuration. From Table 5.4 it can be seen, that there is per level only one nonlinear iteration necessary. In Figure 5.17, the iteration history on Level 9 for both choices of $\boldsymbol{u}_9^0$ is depicted. As can be seen, at the beginng of the nonlinear search phase the algebraic error is reduced substantially. Then, there is a slowdown dircetly before finally identifying the coincidence set. This is due to the coarse grid corrections which have to satisfy constraints in both, tangential and normal direction. This lead to very restrictive constraints for the coarse grid corrections. For completeness, in Figure 5.19, the boundary stresses are depicted. Summarizing, we have seen that for the nonlinear iteration the choice of the start iterate is important. A suitable start iterate is always provided if nested iteration is used. If no start iterate is available, we propose the choice $\boldsymbol{u}_j^0 = \boldsymbol{0}$.

5.6 Truncated Nodal Basis versus Standard Nodal Basis

In this section, we consider an essential difference between scalar obstacle problems and the Signorini problem with varying normals. In particular, we show that for Signorini's problem the use of truncated search directions is necessary for getting multigrid convergence speed. This is in contrast to the scalar case. Here, also standard monotone multigrid

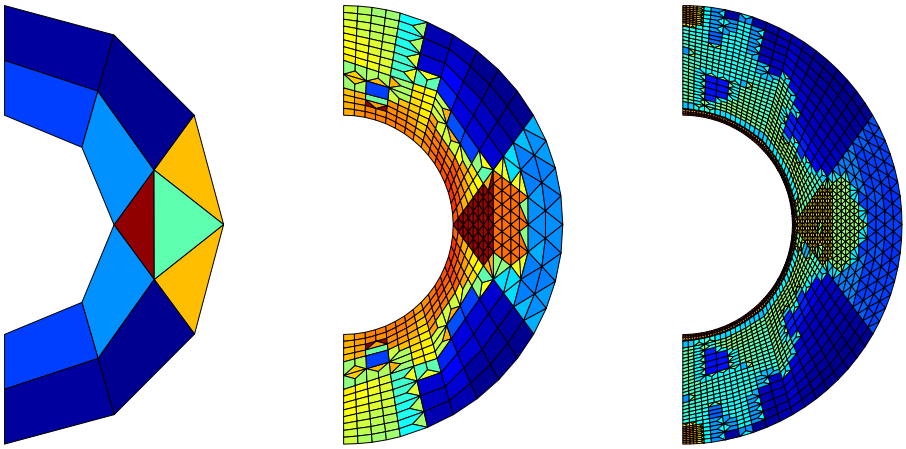

Figure 5.18: Boundary stresses and refinement history for levels $j = 0, 3, 5$.

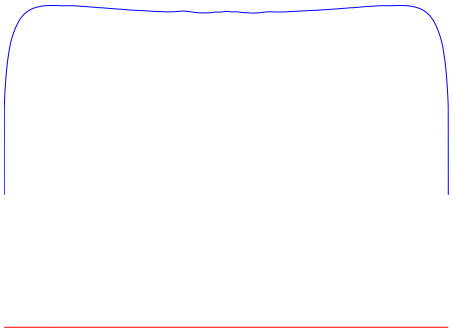

Figure 5.19: Boundary stresses. Normal stresses are blue, tangential stresses are red

methods show multigrid convergence speed, see [Kor97a]. The reason for this different behavior of the method is that for systems of equations the obstaclle directions differ in general. In other words, contact problems with varying normals need the truncated search directions. To illustrate this effect, we consider the twodimensional example presented in Section 5.1. In contrast to Section 5.1, we take the outer normals of the computational domain $\mathscr{B}$ as obstacle direction. That is, the non-penetration condition is given with respect to the outer normals of the body $\mathscr{B}$ in it's reference configuration. We apply an $\mathcal{W}(3,3)$ cycle of the monotone multigrid method with and without truncation of the coarse space basis funtions. As can be seen in the left side of Figure 5.21, the standard splitting shows degenerating asymptotic convergence rates. In contrast, the convergence speed of the method induced by the extended splitting is level independent, see the right side of Figure 5.21 An implicit explanation of this effect has already been given in Section 3.2. Here, we have been given an interpretation of the truncated basis functions in terms of a projection. In particular, the truncated basis functions are constructed in a

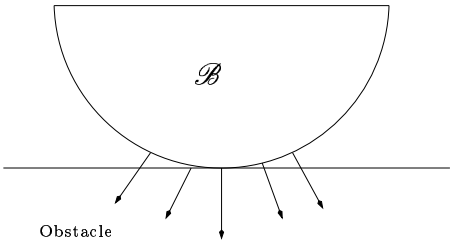

Figure 5.20: Geometry of the test example with varying normals

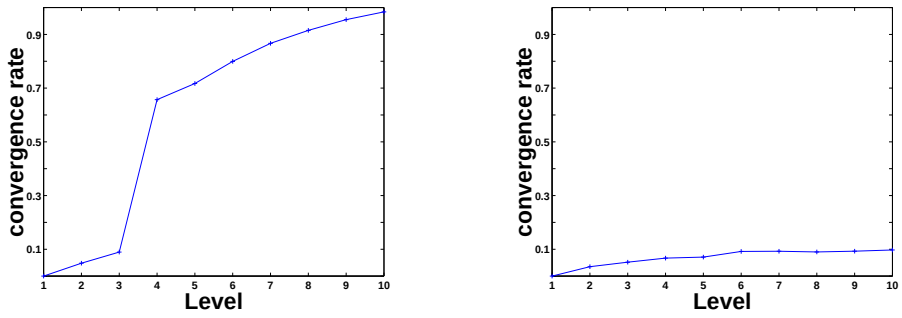

Figure 5.21: Asymptotic convergence rates for the monotone multigrid method using the standard nodal basis (left) and using the truncated basis (right)

way, such that there is no contribution in direction of the obstacle direction. Let us now assume we do not use a truncated basis function, but rather a standard coarse space basis function. Then, as explained in Section 3.2, any correction originating from a standard coarse grid function at the contact boundary has to vanish. Thus, there are no coarse grid correction at the actual contact zone. Our numerical examples show, that already a *single* vanishing coarse grid corrections spoils the convergence of the multigrid method. To be more precise, in this case the approximation property (2.26) is violated, leading to slow convergence of the multigrid method.

Consequently, the particular choice of the extended splitting (3.1) is crucial for the convergence speed of the method. Our numerical examples show, that the extended splitting induced by our truncated basis functions leads to an efficient nonlinear solver. Moreover, it gives rise to a linear method with multigrid convergence speed.

Remark 5.6 *Truncation of coarse grid basis functions is not necessary, if the outer normals are equal. Then, we are in a setting similar to the scalar case. For a comparison of the standard und the truncated monotone multigrid method in the scalar case we refer the reader to [Kor97a]. Anyhow, truncation speeds up convergence, even in case of constant normal directions.*

5.7 Performance of the Parallel Monotone Multigrid Method

In this section, we give an example for solving nonlinear contact problem in three space dimensions adaptively and in parallel. Additionally, in the linear phase we accelerate the convergence by using a conjugate gradient method. This example is intended to illustrate the performance of our method in combination with nested iteration and a Krylov subspace method. As it turns out, the nonlinear overhead of the method is neglectable with respect to the total computational cost. Moreover, using nested iteration the coincidence set is usually identified during the first or second iteration step. Thus, on each level less than than five iterations are sufficient.

The computational domain $\mathscr{B}$ under consideration is the cuboid with lower left and upper right corner $(-1, 0, 0)$ and $(2, 1, 1)$, respectively, see also Figure 5.23. As obstacle, we use a cylinder with diameter 0.4 placed on top of the cuboid, see the left of Figure 5.22. The axis of the cylinder is $\{(x, y, z) \mid -1 \leq x \leq 20, y = 0.5 \leq 1, z = 1.4\}$. Thus, the minimal distance of the obstacle to the body is zero in the reference configuriation. At the side opposite to the cylinder we prescribe Dirichlet conditions $u(x, y, z) = (0, 0, 0.05)$. The side facing the obstacle is the Signorini boundary and homogeneous Neumann boundary conditions are prescribed at the remaining part of the boundary. In Table 5.5, we summarize the results of our numerical experiment. On the coarsest grid, we start with initial iterate zero and then use nested iteration. On each level, the iteration process is stopped, if the the stopping criterion (5.1) is satisfied. Adaptive refinment is used, controlled by an residual based error indicator. The global solution process is stopped, if the estimated error is below 5%. This is the case on Level 5, here we have an estimated relative error of 0.034. Let us emphasize that the solution is obtained by parallel computing. For this example, we use four processors. The final load balancing can be seen in Figure 5.23. The normal stresses are depicted in the right of Figure 5.22. In Table 5.5, the results of

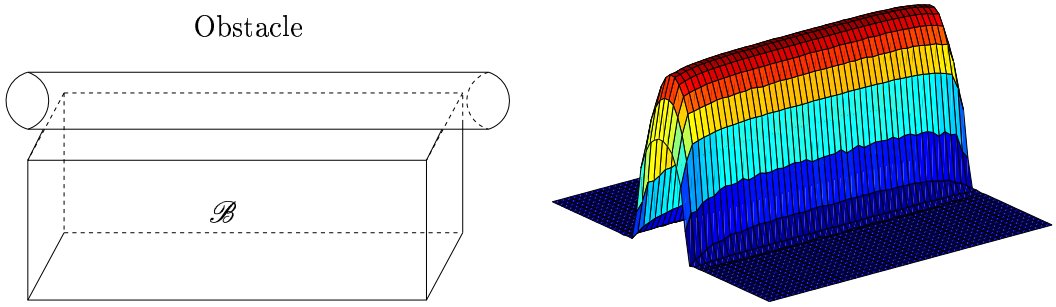

Figure 5.22: Geometry (left) and Normals stresses (right)

our experiment are shown. As can be seen, the total number of iterations is less than five on each level. On Level five, the iteration is stopped before the nonlinear phase of the solution process is finished. We remark that the coincidence set is already identified after two iterations on Levels 5. Here, the iteration is still nonlinear since we have about 20

"contact" nodes on coarse levels $\S k$, $k < 5$. This does not affect the coincidence set nor the convergence speed. The finite element tollbox UGprovides parallel multigrid method, see

Level	# dof	# contact	# nonlin. iter	# total iter
0	375	—	—	—
1	2 187	27	3	5
2	4 557	83	2	4
3	26 424	290	2	4
4	148 596	1 087	2	4
5	354 513	4 164	3	3

Table 5.5: Performance of the nested iteration

[BBJ+97, Bas96] and the references cited therein. In particular, load balancing routines and high level routines providing functionality for the data transfer between the different processors are available. Thus, to parallelize our nonlinear method, we only have to take care of the nonlinearity at the contact boundary. In particular, additional information transfer between the different processors is necessary. This concerns the monotone restrictions as well as the nonlinear Gauß–Seidel scheme and the modification of the coarse grid functions. In parallel computing, the stiffness matrix is distributed onto different processors. Thus, at the processor borders the entries in the stiffness matrix used for parallel computing and the entries in the standard stiffness matrix can differ. For linear problems, different ways of handling the entries of the stiffness matrix at the processor borders are possible. In contrast, the convergence of our nonlinear method relies on these entries being equal, i.e., the matrix entries at the processor borders have to coincide with the entries of the standard matrix. The reason is, that any node the resdiduum with respect to the standard stiffness matrix has to be available, which is necessary for solving the local nonlinear subproblems (3.2). This requirement holds also for the coarse grids matrices. Here, additional data transfer is necessary to obtain the correct matrix entries. We do not discuss this topic in detail here, but emphasize, that in our parallel monotone multigrid method the processor borders can also be in the Signorini boundary, as can be seen in Figure 5.23.

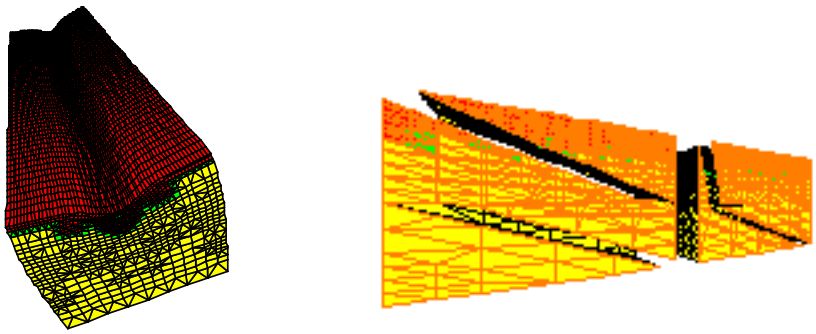

Figure 5.23: Distorted grid on Level 5 (left and load balancing (right).